A STOCHASTIC APPROACH TO UNCERTAINTY IN THE EQUATIONS OF MHD KINEMATICS[*]

EDWARD G. PHILLIPS[†] AND HOWARD C. ELMAN[‡]

Abstract. The magnetohydodynamic (MHD) kinematics model describes the electromagnetic behavior of an electrically conducting fluid when its hydrodynamic properties are assumed to be known. In particular, the MHD kinematics equations can be used to simulate the magnetic field induced by a given velocity field. While prescribing the velocity field leads to a simpler model than the fully coupled MHD system, this may introduce some epistemic uncertainty into the model. If the velocity of a physical system is not known with certainty, the magnetic field obtained from the model may not be reflective of the magnetic field seen in experiments. Additionally, uncertainty in physical parameters such as the magnetic resistivity may affect the reliability of predictions obtained from this model. By modeling the velocity and the resistivity as random variables in the MHD kinematics model, we seek to quantify the effects of uncertainty in these fields on the induced magnetic field. We develop stochastic expressions for these quantities and investigate their impact within a finite element discretization of the kinematics equations. We obtain mean and variance data through Monte-Carlo simulation for several test problems. Toward this end, we develop and test an efficient block preconditioner for the linear systems arising from the discretized equations.

Key words. magnetohydrodynamics, uncertainty quantification, kinematics equations, iterative methods

1. Introduction. Magnetohydrodynamics (MHD) is the study of the interaction between electrically conducting fluids and magnetic fields. The MHD model applies to a range of fluids including plasmas, liquid metals, and brine. The equations governing MHD dynamics result from a coupling of the equations of MHD kinematics and the Navier-Stokes equations for fluid flow through the Lorentz force. In this work, we consider the kinematics equations, which govern the influence of the fluid flow on the magnetic field. These equations constitute a component block within fully coupled MHD simulations [3, 17]. Furthermore, solution of these equations is also required in operator splitting techniques that alternate between solving the Navier-Stokes equations and the kinematics equations [16]. The kinematics equations are also of particular interest in the field of kinematic dynamo theory, in which the ratio of the Lorentz force to inertia is assumed to be small [12]. In this case, the velocity can be prescribed, and the generation of the magnetic energy induced by the flow can be studied. Kinematic simulations can be used to model MHD generators, in which plasmas act as conductors to generate electric currents, as well as natural dynamos such as the sun and the geodynamo. They are of primary interest in investigating whether a given flow profile can sustain dynamo action.

When the velocity field is prescribed, this simplifies the MHD equations, but it may also introduce some epistemic uncertainty into the model. The flow properties of the fluid may not be known on the interior of the domain. Additionally, there are aspects of the physical model that motivate incorporation of small-scale uncertainty. For instance, the large-scale mean flow of the earth's outer core cannot account for the magnitude of the earth's magnetic field. In geodynamo theory, it is proposed that

small-scale turbulent behavior can give rise to a large-scale magnetic field through the α-effect [5]. Furthermore, the distribution of material properties may be uncertain in physical applications. When multiple fluids are present, such as when multiple liquid metals are mixing together, the magnetic resistivity will not be homogeneous throughout the domain and may vary over orders of magnitude. Because the resistivity can have a strong influence on such physical systems, including changing the topology of the magnetic field, we are interested in how uncertain heterogeneous distributions of the resistivity may affect the induced magnetic energy.

In this study, we explore these issues by mathematically simulating uncertainty in both the velocity field and the resistivity within the MHD kinematics model. In this model, we treat the uncertain quantities as random fields correlated in space. We will obtain mean and variance data through Monte-Carlo simulation. In addition, because each Monte-Carlo trial requires the solution of linear systems with randomly varying dynamics, we develop and explore efficient and robust solvers for discrete kinematics systems.

Thus, we consider two issues: the impact of uncertainty of velocity and resistivity on statistical properties of the magnetic fields modeled by the equations of MHD kinematics, together with efficient computational algorithms for computing these quantities. The remainder of the paper is structured as follows. In Section 2, we will derive a finite element formulation for the deterministic equations of MHD kinematics. Section 3 is devoted to the incorporation of uncertainty into the model. In this section, we describe a means of modeling the uncertainty in both the resistivity and the velocity field and apply the model to representative test problems. In Section 4, we propose, analyze, and test a block preconditioner for solving the linear systems arising in our model. Finally, we will draw conclusions in Section 5.

2. A Finite Element Formulation. The steady-state kinematics of MHD are governed by Maxwell's equations

$$\nabla \times \left(\frac{1}{\mu} \vec{B} \right) = \vec{j}, \tag{2.1a}$$

$$\nabla \cdot (\varepsilon \vec{E}) = \rho_c, \tag{2.1b}$$

$$\nabla \times \vec{E} = \vec{0}, \tag{2.1c}$$

$$\nabla \cdot \vec{B} = 0, \tag{2.1d}$$

and Ohm's law

$$\vec{j} = \sigma(\vec{E} + \vec{u} \times \vec{B}), \tag{2.2}$$

on a domain $\mathcal{D} \subset \mathbb{R}^d, d = 2$ or 3 (plus appropriate boundary conditions). The unknowns here are the magnetic induction $\vec{B}$, the electric field $\vec{E}$, and the current density $\vec{j}$; the charge density ρ_c can be regarded as an auxiliary variable obtained after computing $\vec{E}$. We will regard the fluid velocity $\vec{u}$ as given. For many applications, the electric permittivity ε and the magnetic permeability μ do not vary significantly for different fluids [6], so we let ε and μ be fixed scalar constants over the whole domain. However, because the heterogeneities of the electric conductivity σ can be large for different liquid metals, we consider σ to be a prescribed, not necessarily constant function on $\mathcal{D}$.

We consider the boundary conditions

$$\vec{B} \times \vec{n} = \vec{q}, \tag{2.3a}$$

$$\vec{E} \cdot \vec{n} = k, \tag{2.3b}$$

on $\partial\mathcal{D}$. We choose these conditions over the alternative (prescribing $\vec{B} \cdot \vec{n}$ and $\vec{E} \times \vec{n}$) because the requirement on the tangential component of $\vec{B}$ is then the natural Dirichlet condition for the curl-conforming edge elements employed to discretize $\vec{B}$.

A standard simplification of equations (2.1) and (2.2) is obtained by eliminating the variables $\vec{j}$ and $\vec{E}$, yielding the following equations for the kinematics of MHD in terms of $\vec{B}$:

$$\nabla \times \left(\frac{\eta}{\mu} \nabla \times \vec{B} \right) - \nabla \times (\vec{u} \times \vec{B}) = \vec{0}, \tag{2.4a}$$

$$\nabla \cdot \vec{B} = 0, \tag{2.4b}$$

on $\mathcal{D}$, where $\eta = 1/\sigma$ is the magnetic resistivity. A boundary condition such as (2.3a) is required to complete this system. After $\vec{B}$ is obtained from solving equations (2.4), $\vec{E}, \vec{j}$, and ρ_c can be recovered.

As stated, the equations (2.4) are over-determined because there are $d + 1$ equations in d unknowns. In order to make the system well-defined without changing the solution $\vec{B}$, we introduce a Lagrange multiplier r (we refer to this variable as the magnetic pseudo-pressure), and consider the equations

$$\nabla \times \left(\frac{\eta}{\mu} \nabla \times \vec{B} \right) - \nabla \times (\vec{u} \times \vec{B}) + \nabla r = \vec{0}, \tag{2.5a}$$

$$\nabla \cdot \vec{B} = 0, \tag{2.5b}$$

with the boundary conditions (2.3a) and $r = 0$ on $\partial\mathcal{D}$. It can be shown that (2.5) admits the same solution $\vec{B}$ as (2.4) by taking the divergence of equation (2.5a). This yields $\Delta r = 0$ on $\mathcal{D}$, which, with the zero Dirichlet condition on r, implies that $r = 0$ on $\mathcal{D}$.

For developing a weak formulation for this problem, we consider the spaces

$$V_0 = \{\vec{C} \in H(curl, \mathcal{D}) | \vec{C} \times \vec{n} = \vec{0} \text{ on } \partial\mathcal{D}\}, \tag{2.6a}$$

$$V_{\vec{q}} = \{\vec{C} \in H(curl, \mathcal{D}) | \vec{C} \times \vec{n} = \vec{q} \text{ on } \partial\mathcal{D}\}, \tag{2.6b}$$

$$Q_0 = H_0^1(\mathcal{D}). \tag{2.6c}$$

Multiplying the equations (2.5) by test functions $\vec{C} \in V_0$ and $s \in Q_0$, and integrating by parts, we obtain the following weak formulation: Find $(\vec{B}, r) \in V_{\vec{q}} \times Q_0$ such that

$$a(\vec{B}, \vec{C}) + c(\vec{B}, \vec{C}) + b(\vec{C}, r) = 0 \tag{2.7a}$$

$$b(\vec{B}, s) = 0 \tag{2.7b}$$

for all $(\vec{C}, s) \in V_0 \times Q_0$, where the bilinear forms are defined as

$$a(\vec{B}, \vec{C}) = \left(\frac{\eta}{\mu} \nabla \times \vec{B}, \nabla \times \vec{C} \right), \tag{2.8a}$$

$$c(\vec{B}, \vec{C}) = -\left(\vec{u} \times \vec{B}, \nabla \times \vec{C} \right), \tag{2.8b}$$

$$b(\vec{B}, s) = (\vec{B}, \nabla s). \tag{2.8c}$$

3

By integrating by parts the divergence of the magnetic induction $\vec{B}$, we limit the required regularity of $\vec{B}$. This allows the model to include magnetic fields $\vec{B}$ with strong singularities arising from re-entrant corners, which is not feasible for $\vec{B} \in H^1(\Omega)^d$ [4].

We discretize the domain into a shape-regular partition $\mathcal{T}_h$ of quadrilaterals or hexahedra $\{K\}$. Letting $\mathcal{P}_\ell(K)$ be the space of polynomials of degree ℓ on K and $\mathcal{N}_\ell(K)$ the space of Nédélec vector polynomials of the first kind [14] (with $\mathcal{P}_{\ell-1}(K)^d \subset \mathcal{N}_\ell(K) \subset \mathcal{P}_\ell(K)^d$), we consider the finite dimensional spaces

$$V_0^h = \{\vec{C}_h \in V_0 | \vec{C}_{h|K} \in \mathcal{N}_\ell(K), K \in \mathcal{T}_h\}, \tag{2.9a}$$

$$V_{\vec{q}}^h = \{\vec{C}_h \in V_{\vec{q}} | \vec{C}_{h|K} \in \mathcal{N}_\ell(K), K \in \mathcal{T}_h\}, \tag{2.9b}$$

$$Q_0^h = \{s_h \in Q_0 | s_{h|K} \in \mathcal{P}_\ell(K), K \in \mathcal{T}_h\}. \tag{2.9c}$$

Then the discrete formulation is as follows: Find $(\vec{B}_h, r_h) \in V_{\vec{q}}^h \times Q_0^h$ such that

$$a(\vec{B}_h, \vec{C}_h) + c(\vec{B}_h, \vec{C}_h) + b(\vec{C}_h, r_h) = 0 \tag{2.10a}$$

$$b(\vec{B}_h, s_h) = 0 \tag{2.10b}$$

for all $(\vec{C}_h, s_h) \in V_0^h \times Q_0^h$.

Let $\mathbf{B}$ be the vector containing the coefficients of $\vec{B}_h$ with respect to a basis for V_0^h, and let $\mathbf{r}$ be the vector containing the coefficients of r_h with respect to a basis for Q_0^h. Then, the finite element solution of the weak formulation (2.10) can be computed by solving a linear system of saddle point structure,

$$\begin{pmatrix} A + N & D^t \\ D & 0 \end{pmatrix} \begin{pmatrix} \mathbf{B} \\ \mathbf{r} \end{pmatrix} = \begin{pmatrix} f \\ 0 \end{pmatrix}. \tag{2.11}$$

In this equation, f includes boundary data, A is a discretization of the magnetic diffusion operator $\nabla \times (\frac{\eta}{\mu}\nabla \times \cdot)$, N is a discretization of the magnetic convection operator $\nabla \times (\vec{u} \times \cdot)$, D is the discrete (negative) divergence operator, and D^t is the discrete gradient.

We now demonstrate some physical aspects of these equations by applying them to two deterministic example problems. All simulations throughout the paper are implemented using the deal.II finite element library [1] with first order Nédélec elements for $\mathbf{B}$ and bilinear elements for $\mathbf{r}$ (i.e. $\ell = 1$ in (2.9)).

2.1. Example Problem: Hartmann Flow. The Hartmann problem [5] is a classic two-dimensional test problem modeling the flow of an electrically conducting fluid through a channel in the presence of an externally applied transverse magnetic field. We pose this problem on the domain $[-0.5, 0.5]^2$ in the presence of the external magnetic field $\vec{B} = (0, 1)$. The coupled MHD equations admit the exact analytic solution

$$\vec{u} = \left(\frac{\cosh(H/2) - \cosh(Hy)}{\cosh(H/2) - 1}, 0 \right) \tag{2.12a}$$

$$\vec{B} = \left(H\nu \frac{\sinh(Hy) - 2\sinh(H/2)y}{\cosh(H/2) - 1}, 1 \right) \tag{2.12b}$$

for this problem, where $H = \sqrt{\frac{1}{\nu\eta}}$ is the Hartmann number and ν is the kinematic viscosity of the fluid. Representative images of the components of $\vec{u}$ and $\vec{B}$ in the
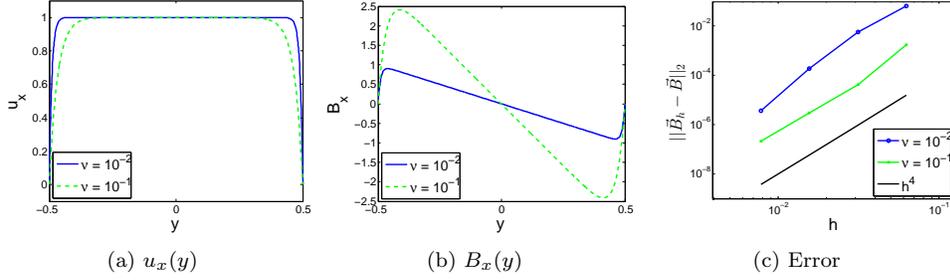
4

(a) $u_x(y)$ (b) $B_x(y)$ (c) Error

Fig. 2.1: Velocity profiles (a), induced magnetic fields (b), and error $||\vec{B}_h - \vec{B}||_2$ (c) for the Hartmann problem.

(a) $\vec{u}$ (b) $\vec{B}_h$ with $\eta = 10^{-3}$ (c) $\vec{B}_h$ with $\eta = 10^{-2}$ (d) $\vec{B}_h$ with $\eta = 10^{-1}$
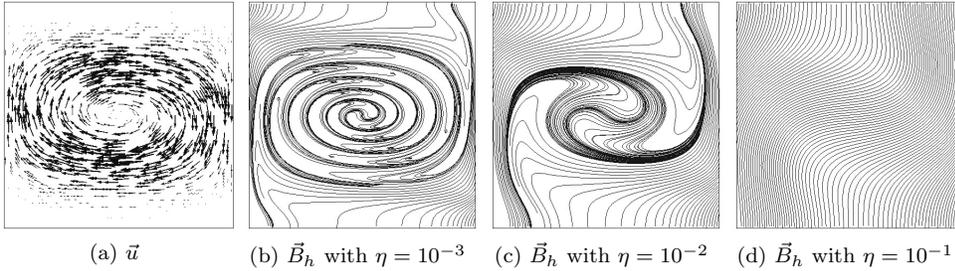
Fig. 2.2: Velocity profile and induced magnetic fields for deterministic MHD eddy problem.

x-direction are plotted in Figure 2.1 for $\eta = 10^{-2}$ and $\mu = 1$ with $\nu = 10^{-1}$ and 10^{-2}. The plots show that smaller viscosity leads to thinner boundary layers in both $\vec{u}$ and $\vec{B}$ and that the magnitude of the induced magnetic field increases with the viscosity. This simple example demonstrates that fairly small changes in the velocity field can lead to large changes in the magnetic field.

We pose a kinematic version of the Hartmann problem by prescribing the velocity defined by (2.12a) over the domain $\mathcal{D}$ and imposing $\vec{B} \times \vec{n} = (0,1) \times \vec{n}$ on the boundary $\partial \mathcal{D}$. The exact solution $\vec{B}$ to this kinematic problem is then given by (2.12b). Applying the finite element formulation (2.10), we obtain the approximation $\vec{B}_h$ to $\vec{B}$. To validate the deterministic finite element formulation, we plot the convergence of the error $||\vec{B}_h - \vec{B}||_2$ as h is refined in Figure 2.1.

2.2. Example Problem: MHD Eddy. The physical effects of the resistivity η are demonstrated by a two-dimensional benchmark problem considered in [12], which models the effect of an eddy on a magnetic field. We prescribe the velocity field

$$\vec{u}(x,y) = \begin{pmatrix} \frac{\cos(\pi x)}{\pi} 32y(1 - 4y^2)^3 \\ -\sin(\pi x)(1 - 4y^2)^4 \end{pmatrix} \tag{2.13}$$

on the domain $\Omega = [-\frac{1}{2}, \frac{1}{2}]^2$ and a vertical magnetic field on the boundary with the condition $\vec{B} \times \vec{n} = (0,1) \times \vec{n}$ on $\partial \mathcal{D}$. Figure 2.2 demonstrates the effect of the resistivity

on the induced magnetic field $\vec{B}$ for three values of η on a 64×64 element mesh. In this figure, we have plotted the velocity profile defined by (2.13) as well as the magnetic field lines for the solution $\vec{B}_h$ with $\eta = 10^{-3}, 10^{-2}$, and 10^{-1}. The figure demonstrates that two competing physical processes are at play in the kinematics model. First, the boundary condition corresponds to an external magnetic field applied to the domain. With infinite resistivity, the velocity field plays no role in the kinematics equations, so the solution is determined solely by the boundary conditions. In this case, this results in the uniform vertical magnetic field $\vec{B} = (0, 1)$. For large resistivity, the solution is dominated by this process. For $\eta = 10^{-1}$ for instance, the solution appears to be a perturbation of the field $\vec{B} = (0, 1)$. The second physical process is governed by the effect of the velocity field on the magnetic field. For small resistivity, the kinematic equations are dominated by the convective term $\nabla \times (\vec{u} \times \vec{B})$ which tends to pull the magnetic field lines in the direction of the velocity field. As the resistivity approaches zero, the topology of the magnetic field then approaches that of the velocity field. For this problem, this means that the magnetic field lines should look more like concentric ellipses as η decreases. This is demonstrated for $\eta = 10^{-3}$, where the magnetic field is nearly "frozen" in the fluid in the center of the domain. Hence, these simulations show that qualitative characteristics of the magnetic topology can indicate the relative resistivity of the system. The more the field lines appear to be pulled by the velocity field (i.e. for this problem, the more swirling in the magnetic field), the smaller the resistivity.

3. MHD Kinematics with Uncertain Data. Because the equations of MHD kinematics may involve uncertain quantities, we propose a formulation that incorporates uncertainty. In particular, we consider the cases where the resistivity η or the velocity field $\vec{u}$ are uncertain. (Because the permeability μ does not vary significantly in applications, we will take it as fixed. Equivalently, we can regard any uncertainty in μ as being absorbed into η.) In this section, we present mathematical representations for each quantity that incorporate uncertainty by treating $\eta = \eta(\omega)$ and $\vec{u} = \vec{u}(\omega)$ as random variables. This yields bilinear forms depending on random variables, i.e.

$$a(\vec{B}, \vec{C}, \omega) = \left(\frac{\eta(\omega)}{\mu} \nabla \times \vec{B}, \nabla \times \vec{C} \right), \tag{3.1a}$$

$$c(\vec{B}, \vec{C}, \omega) = - \left(\vec{u}(\omega) \times \vec{B}, \nabla \times \vec{C} \right), \tag{3.1b}$$

defining a stochastic weak formulation. Thus, by the Doob-Dynkin Lemma, the solution $(\vec{B}_h, r_h)$ is also a random variable defined on the same sample space [15]. Hence, each realization of $\eta(\omega)$ and $\vec{u}(\omega)$ yields the weak formulation: Find $(\vec{B}_h(\omega), r_h(\omega)) \in V_{\vec{q}}^h \times Q_0^h$ such that

$$a(\vec{B}_h(\omega), \vec{C}_h, \omega) + c(\vec{B}_h(\omega), \vec{C}_h, \omega) + b(\vec{C}_h, r_h(\omega)) = 0 \tag{3.2a}$$

$$b(\vec{B}_h(\omega), s_h) = 0 \tag{3.2b}$$

for all $(\vec{C}_h, s_h) \in V_0^h \times Q_0^h$. The solution of any realization of this problem can be obtained by solving a linear system of the form

$$\begin{pmatrix} A(\omega) + N(\omega) & D^t \\ D & 0 \end{pmatrix} \begin{pmatrix} \mathbf{B}(\omega) \\ \mathbf{r}(\omega) \end{pmatrix} = \begin{pmatrix} f \\ 0 \end{pmatrix}. \tag{3.3}$$

Given this framework, we can employ a Monte-Carlo simulation to obtain statistical properties of $\vec{B}_h$. We repeatedly generate independent random instances of $\eta(\omega)$

and $\vec{u}(\omega)$ and solve for $\vec{B}_h(\omega)$. We then estimate the mean and standard deviation of $\vec{B}_h$ by the (pointwise) sample mean, which we denote $\mu(\vec{B}_h)(\vec{x})$, and the sample standard deviation, which we denote $\sigma(\vec{B}_h)(\vec{x})$. A canonical error estimate for Monte-Carlo simulation [2] states that for N trials, the (pointwise) stochastic error for each component of $\mu(\vec{B}_h)$ satisfies

$$|E(B_i(\vec{x},\omega)) - (\mu(\vec{B}_h)(\vec{x}))_i| \approx 2\frac{(\sigma(\vec{B}_h)(\vec{x}))_i}{\sqrt{N}} \qquad (3.4)$$

with 95% confidence. Thus, we obtain with 95% confidence the error result

$$||E(\vec{B}(\vec{x},\omega)) - \mu(\vec{B}_h)(\vec{x})||_2 \approx 2\frac{||\sigma(\vec{B}_h)(\vec{x})||_2}{\sqrt{N}}. \qquad (3.5)$$

3.1. Uncertain Velocity. In this section, we consider the case where fluctuations are allowed in the velocity field. We assume that a mean flow, $\vec{u}_0$, is known and represent the fluctuations by a random variable, $\vec{u}_*(\omega)$, with mean zero. We thus express $\vec{u}$ as the sum of its deterministic and random parts as

$$\vec{u}(\omega) = \vec{u}_0 + \vec{u}_*(\omega). \qquad (3.6)$$

Rather than letting each component of $\vec{u}_*$ be an independent scalar random variable, we derive two expressions for $\vec{u}_*$ from assumptions about physical properties of the fluid, either that the fluctuation is irrotational or that the fluid is incompressible. This results in a natural coupling of the components of $\vec{u}_*$. We explore the effects of an uncertain velocity field on the MHD kinematics system in Sections 3.1.1 and 3.1.2 by applying fluctuations of these types to the Hartmann flow problem detailed in Section 2.1.

3.1.1. Test Problem 1: Irrotational Fluctuations. If the random fluctuations of the fluid are irrotational ($\nabla \times \vec{u}_* = 0$), then $\vec{u}_*$ is a conservative vector field and can be written as the gradient of a scalar potential ϕ, i.e.

$$\vec{u}_* = \nabla\phi. \qquad (3.7)$$

Under this assumption, only the random scalar field ϕ needs to be specified in order to define $\vec{u}$. We assume the potential field to vary continuously and to be spatially correlated. These assumptions are satisfied if we assume ϕ to be a stationary random field with the covariance function defined by

$$C(\vec{x},\vec{y}) = \sigma^2 e^{-\frac{||\vec{x}-\vec{y}||_2}{\ell}}. \qquad (3.8)$$

Here, σ^2 is the variance and ℓ is a correlation length. Clearly, the covariance is greatest when the Euclidean distance between the points $\vec{x}$ and $\vec{y}$ is small. In effect, this covariance function generates fluctuations in ϕ on a scale proportional to ℓ.

If ϕ has mean zero, then ϕ can be approximated by a truncated Karhunen-Loève (KL) expansion [7]

$$\phi(\vec{x},\xi) \approx \sum_{i=1}^{M} \sqrt{\lambda_i}\phi_i(\vec{x})\xi_i, \qquad (3.9)$$
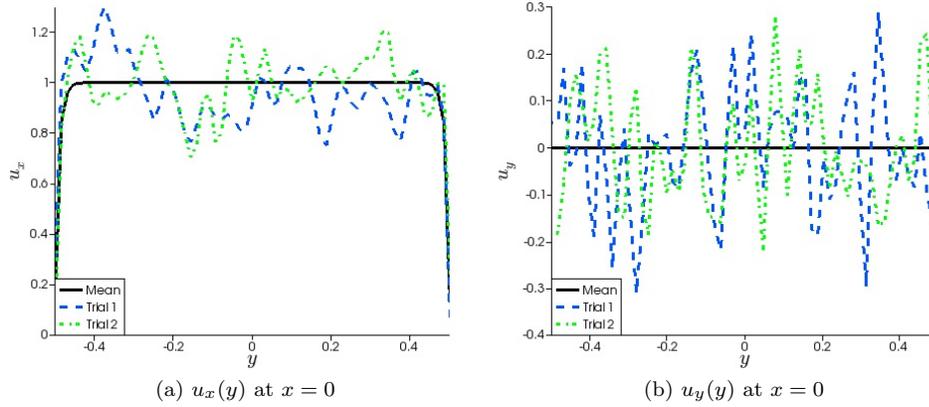
7

(a) $u_x(y)$ at $x = 0$ (b) $u_y(y)$ at $x = 0$

Fig. 3.1: Profiles of u_x and u_y along the line $x = 0$ for two random instances with $\sigma^2 = 5.0 \times 10^{-3}$, together with the mean profile.

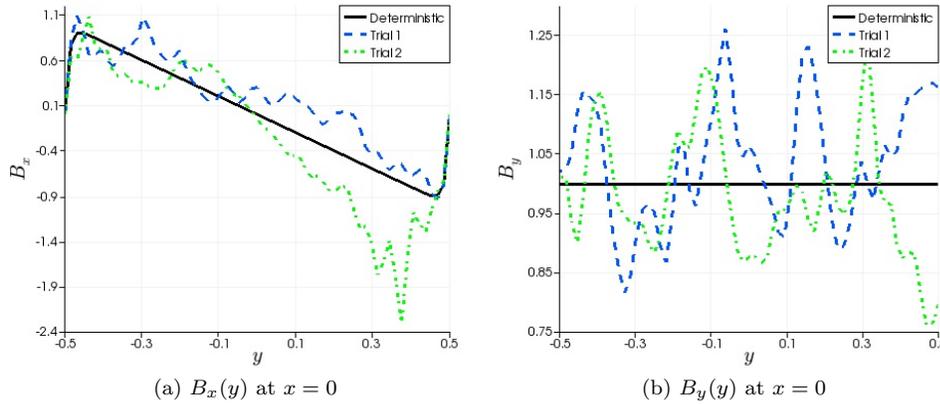(a) $B_x(y)$ at $x = 0$ (b) $B_y(y)$ at $x = 0$

Fig. 3.2: Profiles of B_x and B_y along the line $x = 0$ for two random instances with $\sigma^2 = 5.0 \times 10^{-3}$, together with the deterministic solution obtained from $\vec{u}_0$.

where $\phi_i(\vec{x})$ and λ_k are the eigenfunctions and eigenvalues of C. We will assume the random variables $\{\xi_i\}$ to be independently and uniformly distributed in $[-\sqrt{3}, \sqrt{3}]^M$. We choose M large enough to capture 95% of the total variance [11]; that is,

$$\sum_{i=1}^{M} \lambda_i > 0.95 |\mathcal{D}| \sigma^2. \tag{3.10}$$

We note that the correlation length affects this requirement, with small ℓ leading to large M.

We let the mean velocity profile $\vec{u}_0$ be given by the deterministic Hartmann profile (2.12a) and introduce fluctuations by letting $\vec{u}$ be defined by (3.6) and (3.9) using the
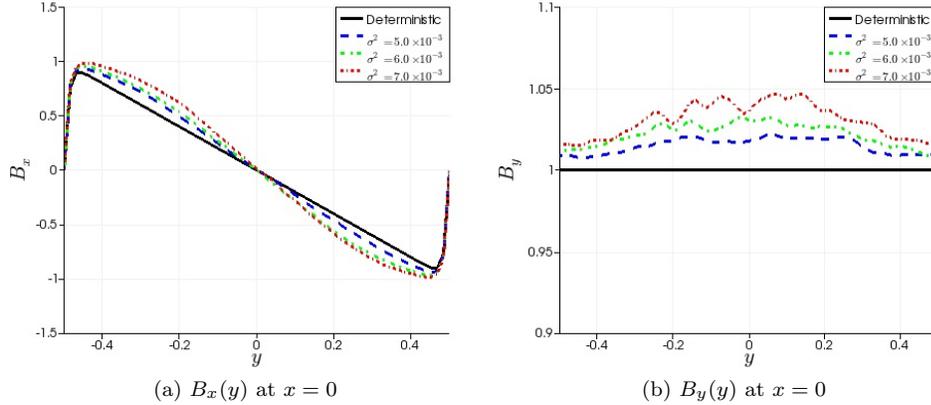
(a) $B_x(y)$ at $x = 0$ (b) $B_y(y)$ at $x = 0$

Fig. 3.3: Profiles of B_x and B_y for Test Problem 1, plotted along the line $x = 0$ for the mean $\mu(\vec{B}_h)$ with $\sigma^2 = 5.0 \times 10^{-3}, 6.0 \times 10^{-3}$, and 7.0×10^{-3}.

covariance function (3.8). We let $\eta \equiv 10^{-2}$, $\nu = 10^{-2}$, and $\ell = 0.1$. This correlation length corresponds to fairly small-scale fluctuations in the velocity field. We compare the effects of three choices for the variance, $\sigma^2 = 5.0 \times 10^{-3}, 6.0 \times 10^{-3}$, and 7.0×10^{-3}. The increase in σ^2 corresponds to an increase in the magnitude of the fluctuations. We present results for this problem discretized on a 64×64 element mesh. Sample random instances of $\vec{u}$ with $\sigma^2 = 5.0 \times 10^{-3}$ are plotted in Figure 3.1. In this figure, the profiles of the components of $\vec{u}$, u_x and u_y, are plotted along the line $x = 0$ and compared to the mean values $(u_0)_x$ and $(u_0)_y$. The corresponding solutions $\vec{B}_h$ are plotted in Figure 3.2. These are compared to the deterministic solution obtained with $\vec{u} \equiv \vec{u}_0$. Both the random data $\vec{u}$ and the corresponding solutions demonstrate high frequency oscillations around the deterministic profiles.

Some results for the Monte-Carlo simulation after 10,000 trials are plotted in Figure 3.3. In this figure, the profiles of the mean solution $\mu(\vec{B}_h)$ are plotted along the line $x = 0$ for the three values of σ^2. This is compared to the deterministic solution $\vec{B}_h$ with $\vec{u} \equiv \vec{u}_0$. The Euclidean norm of the pointwise variance of the solution $||\sigma(\vec{B}_h)(\vec{x})||_2$ is bounded by 0.28 for $\sigma^2 = 5.0 \times 10^{-3}$, 0.38 for $\sigma^2 = 6.0 \times 10^{-3}$, and 0.51 for $\sigma^2 = 7.0 \times 10^{-3}$. By (3.5), this implies that the maximum (pointwise) stochastic error for this problem is approximately 0.01. From Figure 3.3, it can be seen that on average, irrotational fluctuations in the velocity field result in a slight growth in the magnitude of the induced magnetic field as compared to the deterministic case. This growth increases as σ^2 increases.

3.1.2. Test Problem 2: Incompressible Flow. If the fluid is assumed to be incompressible (i.e. $\nabla \cdot \vec{u} = 0$) and $\vec{u}_0$ is incompressible, then $\vec{u}_*$ must also be incompressible (see (3.6)). Thus, in this case, we can prescribe $\vec{u}_*$ to be the curl of a potential ϕ. In two dimensions, ϕ is a scalar, and in three dimensions ϕ is a vector. We consider only the 2D case in this study. Then, $\vec{u}_*$ can be written as

$$\vec{u}_* = \left(\frac{\partial \phi}{\partial y}, -\frac{\partial \phi}{\partial x} \right), \tag{3.11}$$

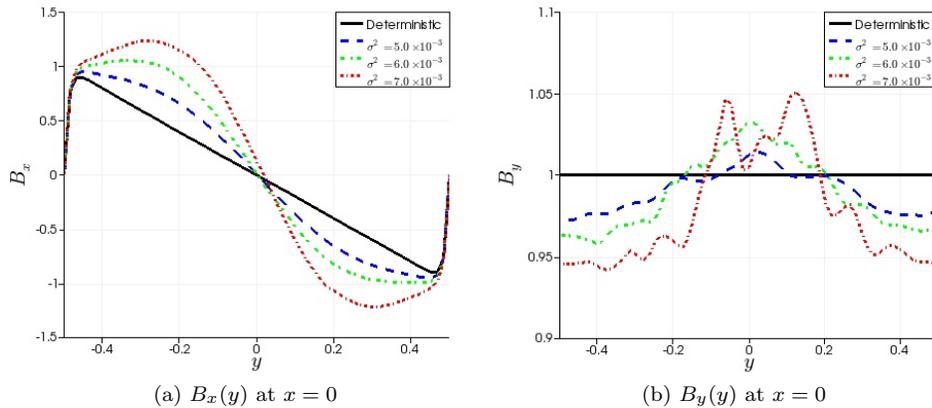(a) $B_x(y)$ at $x = 0$ (b) $B_y(y)$ at $x = 0$

Fig. 3.4: Profiles of B_x and B_y for Test Problem 2, plotted along the line $x = 0$ for the mean $\mu(\vec{B}_h)$ with $\sigma^2 = 5.0 \times 10^{-3}, 6.0 \times 10^{-3}$, and 7.0×10^{-3}.

and the random variable $\vec{u}_*$ can be computed from the scalar random variable ϕ. As above, we let ϕ be defined by a KL expansion (3.9) with the covariance function C. Again, we let $\eta \equiv 10^{-2}$, $\nu = 10^{-2}$, and $\ell = 0.1$ and consider $\sigma^2 = 5.0 \times 10^{-3}, 6.0 \times 10^{-3}$, and 7.0×10^{-3}.

Mean solution profiles obtained from the Monte-Carlo simulation after 10,000 trials are plotted in Figure 3.4. The normed standard deviation $||\sigma(\vec{B}_h)(\vec{x})||_2$ is bounded by 0.49 for $\sigma^2 = 5.0 \times 10^{-3}$, 1.23 for $\sigma^2 = 6.0 \times 10^{-3}$, and 3.17 for $\sigma^2 = 7.0 \times 10^{-3}$, corresponding to a maximum stochastic error of about 0.06. Compared to the case of irrotational fluctuations, both the standard deviation of the solution and the magnitude of the induced magnetic field are greater when non-zero vorticity is permitted in the fluctuations. The difference in the magnitude of the magnetic field is fairly significant between the two test problems, suggesting that fluid vorticity plays a large role in generating magnetic fields. Thus, when small-scale rotational behavior is present in a fluid, simulations based on the mean flow of the fluid may not capture important magnetic effects.

3.2. Uncertain Resistivity. In this section, we consider the case where just the resistivity η is a random field over the domain. This is motivated by the fact that multiple fluids may be present in a physical system and there may be some epistemic uncertainty in the distribution of the fluids throughout the domain. In practical applications, the resistivity can range over orders of magnitude between two fluids. For example, in aluminum electrolysis, the resistivity of liquid aluminum is approximately $4.0 \times 10^{-3}\Omega m$, while the resistivity of the fluid bath from which the aluminum is reduced is approximately $2.9 \times 10^{-7}\Omega m$ [6]. We propose defining

$$\eta(\vec{x}, \omega) = 10^{\beta(\vec{x}, \omega)}, \tag{3.12}$$

where β is a random scalar field yet to be specified. This expression both emphasizes the variability in the order of magnitude of η and guarantees that $\eta > 0$. We first use this to investigate the effects of uncertain resistivity on the MHD eddy problem
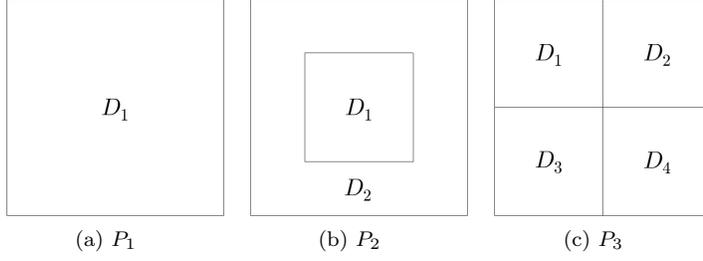
10

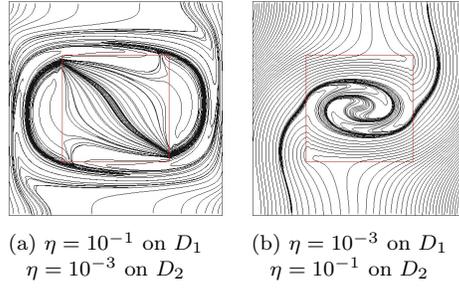Fig. 3.5: Domain partitionings considered in Test Problem 3.

(a) $\eta = 10^{-1}$ on D_1
$\eta = 10^{-3}$ on D_2

(b) $\eta = 10^{-3}$ on D_1
$\eta = 10^{-1}$ on D_2

Fig. 3.6: Instances of $\vec{B}_h$ obtained with partitioning P_2 for Test Problem 3.

discussed in Section 2.2, for two different choices of β. We then consider a three-dimensional extension of the MHD eddy problem

3.2.1. Test Problem 3: Piecewise constant β. In this section, we assume that the domain is occupied by multiple immiscible fluids with different resistivities. In this setting, we let β be a piecewise constant scalar field over the domain. We partition the domain $\mathcal{D}$ into n subdomains $P = \{\mathcal{D}_k\}_{k=1}^n$ and let β be a constant on each of these subdomains. If we assume the resistivity to be uncertain on each of the subdomains, then we can let $\beta(\cdot, \vec{\xi})|_{\mathcal{D}_k} = \xi_k$ where $\vec{\xi} = [\xi_1, \dots, \xi_n]^t$ is a random vector.
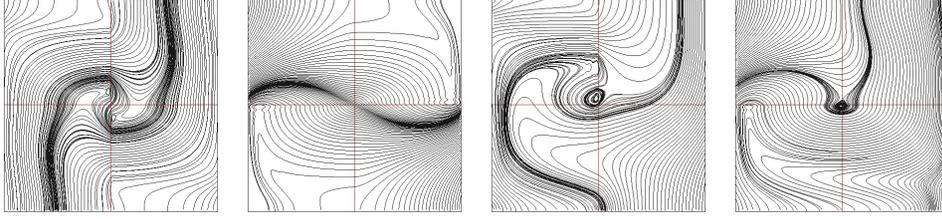
We investigate the effect of a piecewise constant resistivity by considering the MHD eddy problem, defining $\vec{u}$ by (2.13) on the domain $[-\frac{1}{2}, \frac{1}{2}]^2$. We consider three partitionings of the domain:

$$P_1 = \{[-\tfrac{1}{2}, \tfrac{1}{2}]^2\}, \tag{3.13}$$

$$P_2 = \{[-\tfrac{1}{4}, \tfrac{1}{4}]^2, [-\tfrac{1}{2}, \tfrac{1}{2}]^2 \backslash [-\tfrac{1}{4}, \tfrac{1}{4}]^2\}, \tag{3.14}$$
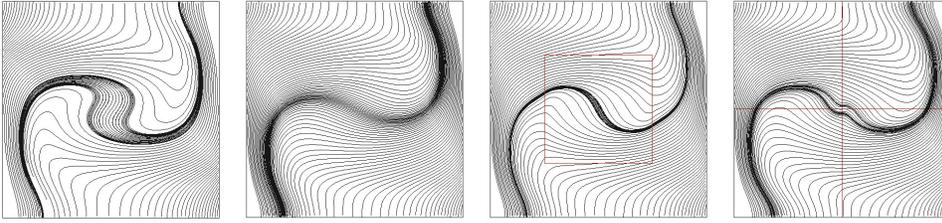
$$P_3 = \{[-\tfrac{1}{2}, 0) \times [0, \tfrac{1}{2}], [0, \tfrac{1}{2}] \times [0, \tfrac{1}{2}], [-\tfrac{1}{2}, 0) \times [-\tfrac{1}{2}, 0), [0, \tfrac{1}{2}] \times [-\tfrac{1}{2})\}, \tag{3.15}$$

as shown in Figure 3.5. We let each ξ_i be independently and uniformly distributed in the interval $[-1.0, -3.0]$. Defining η by (3.12), we obtain $E(\eta) \equiv \eta_0 \approx 2.1 \times 10^{-2}$ independent of the partitioning. With partitioning P_1, the resistivity is a random constant over the domain. Thus, the solutions plotted in Figure 2.2 are representative instances of magnetic fields that may be induced for this partitioning. With partitioning P_2, the resistivity in the center of the domain may differ from the resistivity

(a) $\eta = 10^{-3}$ on D_1, D_4 (b) $\eta = 10^{-3}$ on D_2, D_3 (c) $\eta = 10^{-3}$ on D_1, D_3 (d) $\eta = 10^{-3}$ on D_3, D_4
$\eta = 10^{-1}$ on D_2, D_3 $\eta = 10^{-1}$ on D_1, D_4 $\eta = 10^{-1}$ on D_2, D_4 $\eta = 10^{-1}$ on D_1, D_2

Fig. 3.7: Instances of $\vec{B}_h$ obtained with partitioning P_3 for Test Problem 3.

(a) $\vec{B}_h$ with $\eta \equiv \eta_0$ (b) $\mu(\vec{B}_h)$ for P_1 (c) $\mu(\vec{B}_h)$ for P_2 (d) $\mu(\vec{B}_h)$ for P_3

Fig. 3.8: Deterministic and mean magnetic field lines compared for Test Problem 3.

near the boundaries, and this can result in in different kinds of behavior than seen for a constant resistivity. Two examples of the kind of behavior we may obtain are plotted in Figure 3.6. In the first example, the resistivity is much larger in the center subdomain, and one can see that the behavior of the magnetic field is more characteristic of a larger resistivity in the center. Near the boundary of $\mathcal{D}$, the field lines are similar to those obtained with $\eta = 10^{-3}$ on the entire domain. Around the interface of the two subdomains, the character of the field lines shifts. The second example in Figure 3.6 shows the opposite case, where the resistivity is smaller in the center subdomain. In this case, one can see behavior characteristic of a large resistivity near the boundary of $\mathcal{D}$ and behavior characteristic of a small resistivity in the center. Figure 3.7 depicts some examples of magnetic fields that can result from partitioning P_3. As with partitioning P_2, it can be seen that the character of the field lines in a particular subdomain are characteristic of the resistivity on that subdomain, and at subdomain interfaces there is a shift in the character of the magnetic field. Figures 3.6 and 3.7 demonstrate not only that a discontinuous resistivity can produce profoundly different solutions than a constant resistivity, but also that the resistivity in a particular region can be approximated by considering the character of the field lines in that region.

Some results for the Monte-Carlo simulation after 10,000 trials on a 64×64 element mesh are shown in Figures 3.8 and 3.9. The field lines for the deterministic case where $\eta = E(\eta(\omega))$ are compared to those obtained from the mean $\mu(\vec{B}_h)(\vec{x})$ in Figure 3.8, and the norm of the standard deviation $||\sigma(\vec{B}_h)||_2$ is plotted in Figure 3.9. Note that
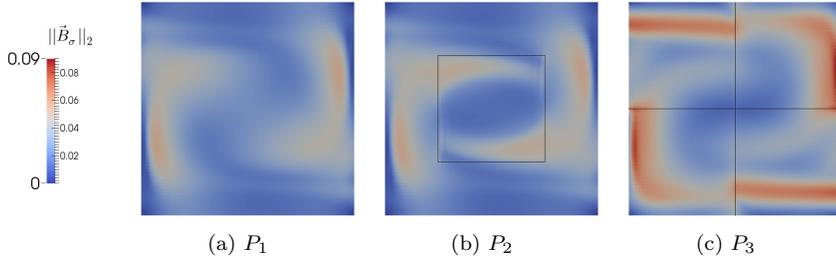
(a) P_1 (b) P_2 (c) P_3

Fig. 3.9: Euclidean norm of standard deviation $||\sigma(\vec{B}_h)||_2$ for Test Problem 3.

the probability that the resistivity is greater than the mean resistivity ($Pr(\eta > \eta_0) \approx 0.33$) is less than the probability that the resistivity is less than the mean resistivity ($Pr(\eta < \eta_0) \approx 0.67$). Despite this, the mean field lines in each example resemble ones that would arise with $\eta > \eta_0$. Because this effect occurs for partitioning P_1, it appears that it is due primarily to the variability of η. When the resistivity is allowed to vary for this test problem, the mean magnetic field is dominated by the qualities of magnetic fields induced by larger resistivities. Figure 3.8 shows that the large-scale behavior of the mean magnetic field is very similar for the three partitionings, although some small-scale differences are present. For partitioning P_2, the behavior in the center subdomain is consistent with a slightly smaller resistivity than in the rest of the domain. With partitioning P_3, the field lines appear to correspond to a larger resistivity around the origin where the four subdomains meet. The results suggest that variability in the resistivity has a more significant effect on the mean magnetic field than the presence of multiple fluids with different resistivities. Although multiple resistivities may result in random instances of $\vec{B}$ that differ significantly from a constant resistivity, as shown in Figures 3.6 and 3.7, the means do not differ dramatically from solutions for constant resistivities, with the main differences arising at subdomain interfaces.

Figure 3.9 shows the norm of the standard deviation of $\vec{B}_h$ over the domain. Because $||\sigma(\vec{B}_h)(\vec{x})||_2 \leq 0.09$, we know from (3.5) that the stochastic error is bounded as

$$||E(\vec{B}_h(\vec{x}, \omega)) - \mu(\vec{B}_h)(\vec{x})||_2 \leq 2\frac{0.09}{\sqrt{10{,}000}} = 1.8 \times 10^{-3} \qquad (3.16)$$

with 95% confidence. From the figure, it can be seen that the standard deviation is affected by the partitioning of the domain. In this case, the standard deviation increases as the number of subdomains increases. The average standard deviation over the domain for partitionings P_1, P_2, and P_3 is approximately $2.9 \times 10^{-2}, 3.0 \times 10^{-2}$, and 4.1×10^{-2}. Furthermore, the standard deviation tends to be larger along the subdomain interfaces.

3.2.2. Test Problem 4: β as a truncated KL expansion. In this section, we assume that the resistivity of the system varies continuously over space. This situation may arise when fluids can blend together, such as when different liquid metals are combined into an alloy. This scenario can be modeled by supplying β with the spatially correlated covariance function C of (3.8). If β has mean $\beta_0(\vec{x})$, then the
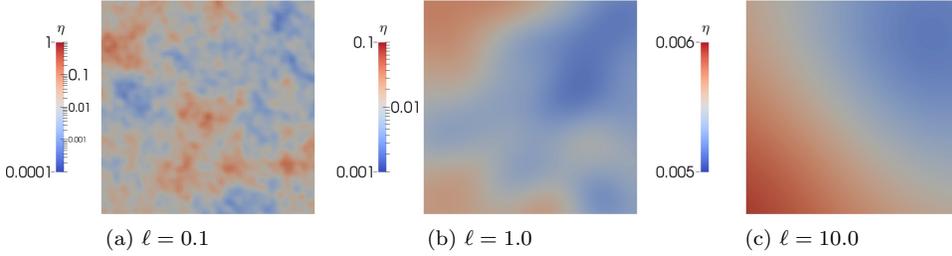
13

(a) $\ell = 0.1$ (b) $\ell = 1.0$ (c) $\ell = 10.0$

Fig. 3.10: Random realizations of η for Test Problem 4.

(a) $\vec{B}_h$ with $\eta \equiv \eta_0$ (b) $\mu(\vec{B}_h)$ with $\ell = 0.1$ (c) $\mu(\vec{B}_h)$ with $\ell = 1.0$ (d) $\mu(\vec{B}_h)$ with $\ell = 10.0$
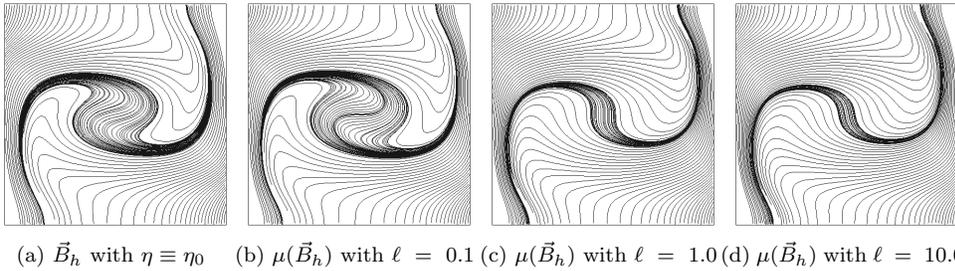
Fig. 3.11: Deterministic and mean magnetic field lines compared for Test Problem 4.

truncated KL expansion for β can be written as

$$\beta(\vec{x}, \xi) \approx \beta_0(\vec{x}) + \sum_{i=1}^{M} \sqrt{\lambda_i} \beta_i(\vec{x}) \xi_i. \tag{3.17}$$

We assume the random variables $\{\xi_i\}$ to be independently and uniformly distributed in $[-\sqrt{3}, \sqrt{3}]^M$ and choose M large enough to capture 95% of the total variance.

We consider the domain $[-\frac{1}{2}, \frac{1}{2}]^2$ and prescribe the velocity field (2.13) with η defined by (3.12). We let β have mean $\beta_0 = -2.0$ and variance $\sigma^2 = 0.4$. This defines the mean of η to be $E(\eta(\omega)) = \eta_0 \approx 1.5 \times 10^{-2}$ (note that $\eta_0 \neq 10^{E(\beta)}$). We discretize the problem on a 64×64 element mesh. We consider three choices of correlation length $\ell = 0.1, 1.0,$ and 10.0 resulting in truncated KL expansions of length 1834, 39, and 2. Representative realizations of β are plotted in Figure 3.10 for these choices. The plots demonstrate that as ℓ increases the resistivity varies over a smaller range for a given realization. Realizations with $\ell = 0.1$, thus, represent heterogeneous systems in which fluids with disparate resistivities have not been mixed well. As ℓ increases the realizations become more homogeneous in resistivity, corresponding to later stages in a mixing process. With $\ell = 10.0$, η varies over a very small range in a particular instance, and in this respect it is similar to the constant resistivity obtained for Test Problem 3 with partitioning P_1. Thus, large correlation lengths correspond to an uncertain final resistivity at the end of a mixing process.

Figures 3.11 and 3.12 show some results of the Monte-Carlo simulation after 10,000 trials. Figure 3.11 shows the magnetic field lines associated with the mean
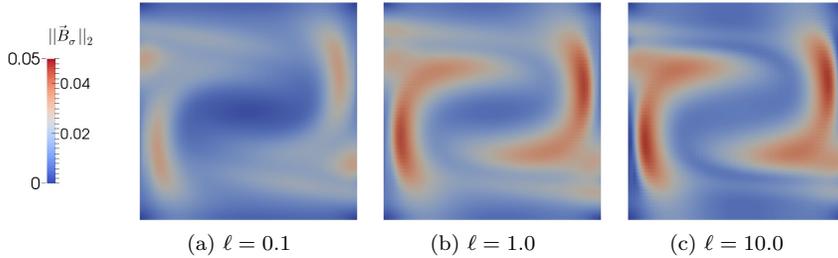
(a) $\ell = 0.1$ (b) $\ell = 1.0$ (c) $\ell = 10.0$

Fig. 3.12: Euclidean norm of standard deviation $||\sigma(\vec{B}_h)||_2$ for Test Problem 4.

of $\vec{B}_h$ with each value of ℓ. These results are compared with the solution to the deterministic problem for $\eta \equiv \eta_0$. It can be seen that with $\ell = 0.1$, the mean field lines are very similar to the field lines obtained from the deterministic problem. As ℓ increases, the field lines differ more from the deterministic solution. In fact, the behavior exhibited for larger ℓ appears to result from a resistivity greater than the mean resistivity η_0; that is, as ℓ increases, the magnetic field lines are drawn more toward the infinite resistivity solution $\vec{B} = (0, 1)$.

Figure 3.12 shows the norm of the standard deviation of $\vec{B}_h$ over the domain. Because $||\sigma(\vec{B}_h)(\vec{x})||_2 \leq 0.05$, the stochastic error is bounded above by 1.0×10^{-3} with 95% confidence. From this figure, it can be seen that the standard deviation increases as ℓ increases. For small ℓ, the mean solution is not only more similar to the deterministic solution, but the standard deviation is also smaller. This suggests that the induced magnetic field is more responsive to variations in the resistivity of homogeneous systems than to small-scale variations in the resistivity of heterogeneous systems. Although the resistivity can vary over a very large range in a heterogeneous system, the fluctuations within random instances have little effect on the induced magnetic field. On the other hand, profound differences from the deterministic case are seen when the resistivity of a homogeneous system is uncertain. This is consistent with the results obtained for Test Problem 3, where we found that variability in the resistivity had stronger effects on the mean solution than the presence of multiple resistivities.

3.2.3. Test Problem 5: Uncertain Resistivity in 3D. In this section, we examine the behavior of solutions obtained for three-dimensional models with uncertain piecewise constant resistivity. We take as our domain the cube $[-\frac{1}{2}, \frac{1}{2}]^3$, and consider a generalization of the velocity field (2.13) in which the component in the z-direction is identically 1,

$$\vec{u}(x, y, z) = \begin{pmatrix} \frac{\cos(\pi x)}{\pi} 32y(1 - 4y^2)^3 \\ -\sin(\pi x)(1 - 4y^2)^4 \\ 1 \end{pmatrix}, \tag{3.18}$$

which describes a swirling flow in the z-direction. Again, we prescribe a magnetic field in the y-direction for the boundary condition, $\vec{B} \times \vec{n} = (0, 1, 0) \times \vec{n}$.

We define the resistivity by (3.12) using piecewise constant β on the partitionings

$$P_1 = \{[-\tfrac{1}{2}, \tfrac{1}{2}]^3\}, \tag{3.19}$$

$$P_2 = \{[-\tfrac{1}{4}, \tfrac{1}{4}]^2 \times [-\tfrac{1}{2}, \tfrac{1}{2}], ([-\tfrac{1}{2}, \tfrac{1}{2}]^2 \backslash [-\tfrac{1}{4}, \tfrac{1}{4}]^2) \times [-\tfrac{1}{2}, \tfrac{1}{2}]\}. \tag{3.20}$$

(a) $\vec{B}_h$ at $z = -\frac{1}{4}$ (b) $\vec{B}_h$ at $z = 0$ (c) $\vec{B}_h$ at $z = \frac{1}{4}$

(d) $\mu(\vec{B}_h)$ at $z = -\frac{1}{4}$ for (e) $\mu(\vec{B}_h)$ at $z = 0$ for P_1 (f) $\mu(\vec{B}_h)$ at $z = \frac{1}{4}$ for P_1
P_1

(g) $\mu(\vec{B}_h)$ at $z = -\frac{1}{4}$ for (h) $\mu(\vec{B}_h)$ at $z = 0$ for P_2 (i) $\mu(\vec{B}_h)$ at $z = \frac{1}{4}$ for P_2
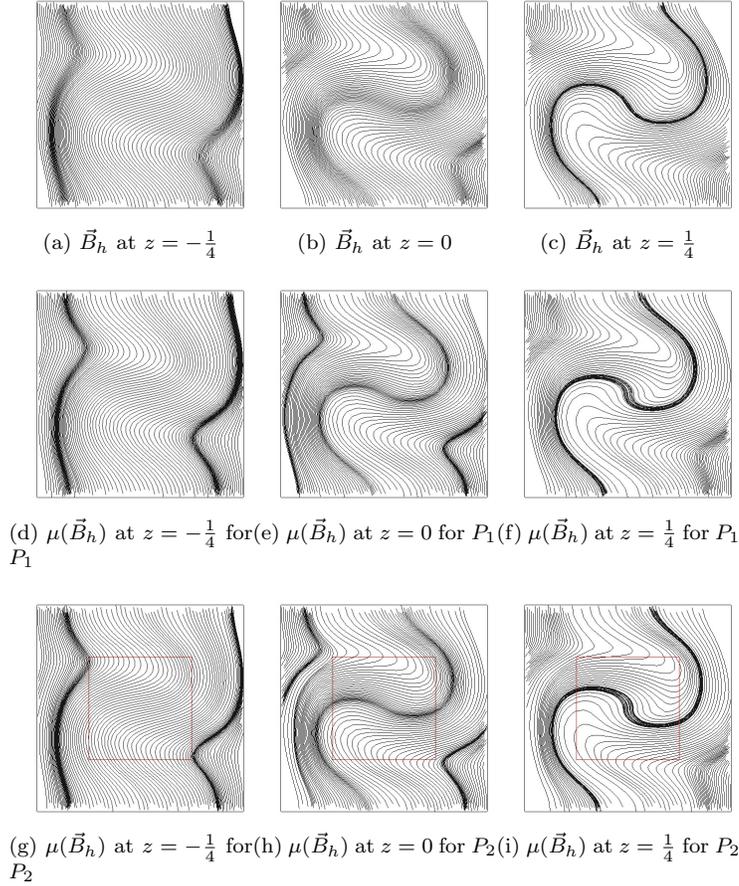P_2

Fig. 3.13: Deterministic fields lines (top), mean field lines with partitioning P_1 (middle), and mean field lines with partitioning P_2 at cross sections $z = -\frac{1}{4}$ (left), $z = 0$ (middle), and $z = \frac{1}{4}$ (right) for Test Problem 5.

These are extensions of partitionings P_1 and P_2 from Test Problem 3 in the z-direction. On each subdomain $\mathcal{D}_k$, we let $\beta(\cdot, \vec{\xi})|_{\mathcal{D}_k} = \xi_k$ where ξ_k is uniformly distributed in $[-1.0, -3.0]$. The mean resistivity in this case is $\eta_0 \approx 2.2 \times 10^{-2}$. Field lines of the sample mean computed from 1,000 Monte-Carlo simulations on a $16 \times 16 \times 16$ element mesh are compared to deterministic field lines for $\eta \equiv \eta_0$ in Figure 3.13. Field lines are computed in the x-y cross sections at $z = -\frac{1}{4}, 0$, and $\frac{1}{4}$. From the deterministic field lines, it can be seen that near the bottom of the domain, the magnetic field is more dominated by the infinite resistivity solution $\vec{B} = (0, 1, 0)$, but as z increases the velocity field has a larger effect on the magnetic field. Comparing to the two-dimensional case, this is as if the resistivity decreases as z increases. We see the same effect for the mean solution. Unlike for the 2D test problems, the mean magnetic field looks like a deterministic solution with $\eta < \eta_0$. Comparing the mean field lines obtained for the two different partitionings, differences due to the multiple resistivities present in partitioning P_2 are very slight. As in 2D, this shows that the
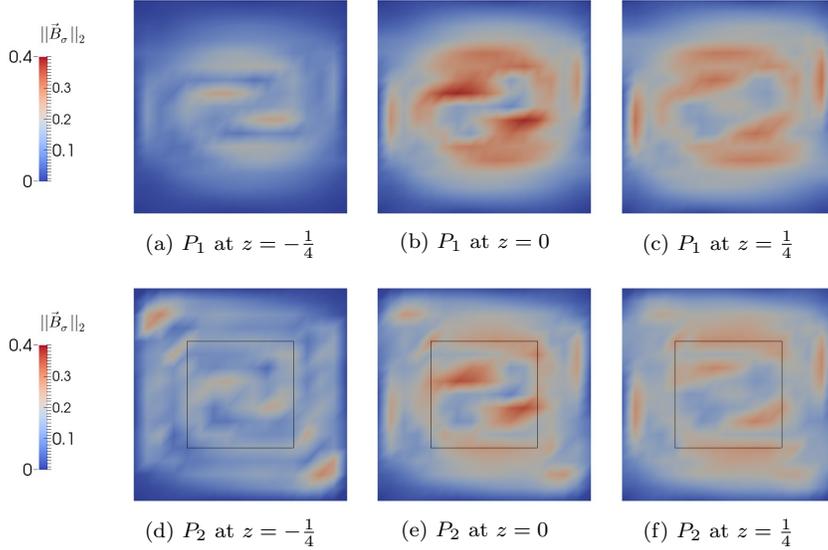
(a) P_1 at $z = -\frac{1}{4}$ (b) P_1 at $z = 0$ (c) P_1 at $z = \frac{1}{4}$

(d) P_2 at $z = -\frac{1}{4}$ (e) P_2 at $z = 0$ (f) P_2 at $z = \frac{1}{4}$

Fig. 3.14: $||\sigma(\vec{B}_h)(\vec{x})||_2$ at cross sections for partitionings P_1 (top) and P_2 (bottom) for Test Problem 5.

effects of variability in the resistivity are stronger than the effects of discontinuities in the resistivity. Cross sections of the norm of the standard deviation are plotted in Figure 3.14. This shows that variability in the magnetic field is greatest at the center cross section $z = 0$. Furthermore, the figure demonstrates that, as in Test Problem 3, a greater number of subdomains leads to a larger standard deviation that is distributed throughout more of the domain.

4. Linear Solvers for the Discretized Kinematics System. In Monte-Carlo simulation, for each realization of the uncertain quantities, a linear system of the form $\mathcal{A}x = b$ must be solved, where

$$\mathcal{A} = \mathcal{A}(\omega) = \begin{pmatrix} A(\omega) + N(\omega) & D^t \\ D & 0 \end{pmatrix}. \tag{4.1}$$

Because many realizations are required to produce accurate statistical results, it is imperative that the linear solver be efficient and robust over random variations in the parameters η and $\vec{u}$. The linear systems are sparse, nonsymmetric and indefinite, and, depending on the level of spatial refinement, they can be very large. Hence, a preconditioned iterative method such as preconditioned GMRES is a natural choice of solver for these systems. Motivated by the results of [13], many successful block preconditioners have been developed for solving similar saddle point systems. Following this line of research, we develop a generalization of a preconditioner proposed in [8] for the time-harmonic Maxwell equations to be used for the discretized kinematics equations.

The system studied in [8] can be considered a special case of (2.5) in which $\frac{\eta}{\mu} \equiv 1$ and $\vec{u} \equiv 0$. If we let $\hat{A}$ be a discretization of the unscaled magnetic diffusion operator

$\nabla \times \nabla \times$, then the coefficient matrix of the resulting linear system can be written

$$\hat{\mathcal{A}} = \begin{pmatrix} \hat{A} & D^t \\ D & 0 \end{pmatrix}. \tag{4.2}$$

The preconditioner developed in [8] is of the form

$$\hat{\mathcal{P}} = \begin{pmatrix} Q_{\mathbf{B}} + \hat{A} & 0 \\ 0 & L_{\mathbf{r}} \end{pmatrix}, \tag{4.3}$$

where $Q_{\mathbf{B}}$ is the mass matrix for $\mathbf{B}$ and $L_{\mathbf{r}}$ is a discrete Laplacian on the magnetic pseudo-pressure space. A generalization of this preconditioner for use with the system $\mathcal{A}$ is

$$\mathcal{P}_k = \begin{pmatrix} kQ_{\mathbf{B}} + A + N & 0 \\ 0 & \frac{1}{k}L_{\mathbf{r}} \end{pmatrix}, \tag{4.4}$$

where $k > 0$ is a constant to be specified.

4.1. Analysis of Eigenvalues. We give a complete analysis of this preconditioner for the case where $N \equiv 0$. The performance of preconditioner $\mathcal{P}_k$ for system $\mathcal{A}$ is governed by the eigenvalues λ of the generalized eigenvalue problem

$$\begin{pmatrix} A & D^t \\ D & 0 \end{pmatrix} \begin{pmatrix} \mathbf{B} \\ \mathbf{r} \end{pmatrix} = \lambda \begin{pmatrix} kQ_{\mathbf{B}} + A & 0 \\ 0 & \frac{1}{k}L_{\mathbf{r}} \end{pmatrix} \begin{pmatrix} \mathbf{B} \\ \mathbf{r} \end{pmatrix}. \tag{4.5}$$

Defining $n = \dim(\mathbf{B})$ and $m = \dim(\mathbf{r})$, this has a total of $n + m$ eigenvalues. From the bottom row of (4.5), we obtain $\mathbf{r} = \frac{k}{\lambda}L_{\mathbf{r}}^{-1}D\mathbf{B}$. Substituting this into the top row of (4.5) gives

$$\lambda A\mathbf{B} + kD^t L_{\mathbf{r}}^{-1}D\mathbf{B} = \lambda^2(kQ_{\mathbf{B}} + A)\mathbf{B}. \tag{4.6}$$

Through a discrete Hodge decomposition, $\mathbf{B}$ can be written as the sum of its discrete curl-free part $\mathbf{B}_A$ and its discrete divergence-free part $\mathbf{B}_D$ (i.e. $\mathbf{B} = \mathbf{B}_A + \mathbf{B}_D$, where $A\mathbf{B}_A = A^t\mathbf{B}_A = 0$ and $D\mathbf{B}_D = 0$). Then (4.6) can be rewritten as

$$\lambda A\mathbf{B}_D + kD^t L_{\mathbf{r}}^{-1}D\mathbf{B}_A = \lambda^2 kQ_{\mathbf{B}}(\mathbf{B}_A + \mathbf{B}_D) + \lambda^2 A\mathbf{B}_D. \tag{4.7}$$

Let the norm induced by a symmetric positive definite matrix X be denoted $||\cdot||_X = \langle X\cdot, \cdot\rangle^{1/2}$. Taking the inner product of (4.7) with $\mathbf{B}_A$ and using the relations

$$\langle Q_{\mathbf{B}}\mathbf{B}_A, \mathbf{B}_D\rangle = \langle Q_{\mathbf{B}}\mathbf{B}_D, \mathbf{B}_A\rangle = 0, \tag{4.8a}$$

$$\langle D^t L_{\mathbf{r}}^{-1}D\mathbf{B}_A, \mathbf{B}_A\rangle = ||\mathbf{B}_A||_{Q_{\mathbf{B}}}^2, \tag{4.8b}$$

proven in [8], we have

$$k||\mathbf{B}_A||_{Q_{\mathbf{B}}}^2 = \lambda^2 k||\mathbf{B}_A||_{Q_{\mathbf{B}}}^2. \tag{4.9}$$

Because there are at least m linearly independent vectors satisfying $\mathbf{B}_A \neq 0$, this means that (4.5) has eigenvalues $\lambda = \pm 1$ each with multiplicity at least m.

Insight into the remaining $n - m$ eigenvalues can be obtained by taking the inner product of $\hat{\mathbf{B}}_D$ with (4.7), yielding

$$\lambda k||\mathbf{B}_D||_{Q_{\mathbf{B}}}^2 = (1 - \lambda)||\mathbf{B}_D||_A^2. \tag{4.10}$$

18

From this equation, it is clear that $0 \leq \lambda \leq 1$. These eigenvalues can be further bounded using the discrete coercivity condition. In [8], this condition is written in terms of the unscaled norm $|| \cdot ||_{\hat{A}}$ as

$$||\mathbf{B}_D||_{\hat{A}}^2 \geq \alpha \left(||\mathbf{B}_D||_{\hat{A}}^2 + ||\mathbf{B}_D||_{Q_\mathbf{B}}^2 \right), \tag{4.11}$$

where the constant $\alpha \in (0,1)$ is independent of the mesh. It can be shown that

$$\tfrac{\eta_m}{\mu} ||\mathbf{B}_D||_{\hat{A}}^2 \leq ||\mathbf{B}_D||_A^2 \leq \tfrac{\eta_M}{\mu} ||\mathbf{B}_D||_{\hat{A}}^2, \tag{4.12}$$

where $\eta_m = \min_{\vec{x} \in \mathcal{D}}\{\eta(\vec{x})\}$ and $\eta_M = \max_{\vec{x} \in \mathcal{D}}\{\eta(\vec{x})\}$, from which we can obtain the coercivity condition in terms of the scaled norm $|| \cdot ||_A$:

$$||\mathbf{B}_D||_A^2 \geq \alpha \left(\tfrac{\eta_m}{\eta_M} ||\hat{\mathbf{B}}_D||_A^2 + \tfrac{\eta_m}{\mu} ||\mathbf{B}_D||_{Q_\mathbf{B}}^2 \right). \tag{4.13}$$

Applying this inequality to (4.10), we obtain

$$\frac{1}{1 + \frac{k\mu}{\alpha\eta_m} \frac{\eta_M - \alpha\eta_m}{\eta_M}} \leq \lambda \leq 1. \tag{4.14}$$

The constant $\frac{\eta_M - \alpha\eta_m}{\eta_M}$ is necessarily smaller than 1; thus, we can write the weaker bound

$$\frac{1}{1 + \frac{k\mu}{\alpha\eta_m}} < \lambda \leq 1. \tag{4.15}$$

If we let $k = \frac{\eta_m}{\mu}$, this bound depends only on the coercivity constant α. This dependence on α is similar to that obtained in [8] for $\hat{\mathcal{A}}$ preconditioned by $\hat{\mathcal{P}}$. Because α is independent of the mesh, letting $k = \frac{\eta_m}{\mu}$ defines a preconditioner which should be robust with respect to both mesh refinement and variations in the resistivity.

When $N \neq 0$, much of the same analysis applies. Because $\mathbf{B}_A$ is curl-free, N satisfies $\langle N\mathbf{B}, \mathbf{B}_A \rangle = 0$. Given this relationship, the presence of N does not affect the two eigenvalues $\lambda = \pm 1$ with multiplicity m. However, the remaining eigenvalues are approximated by

$$\left(\lambda \left(\tfrac{\eta_m}{\mu} + k \right) - k \right) |\mathbf{B}_D|_{Q_\mathbf{B}}^2 = (1 - \lambda) \left(|\mathbf{B}_D|_A^2 + \langle N\mathbf{B}, \mathbf{B}_D \rangle \right). \tag{4.16}$$

Because $\langle N\mathbf{B}, \mathbf{B}_D \rangle$ can become negative, it is difficult to say more about these eigenvalues, but in practice, this preconditioner proves to be effective. This will be demonstrated in the following section.

4.2. Numerical Results. Because the number of preconditioned GMRES iterations required for convergence depends on the linear system obtained from the random data $\vec{u}(\omega)$ and $\eta(\omega)$, we can regard these iteration counts as a random variable. Consequently, we obtain an estimate of the mean of the number of iterations required for convergence using the sample mean from a Monte-Carlo simulation. The GMRES iteration continues until the stopping criterion

$$||b - \mathcal{A}x|| \leq 10^{-8} ||b|| \tag{4.17}$$

is satisfied. We compute the average number of iterations to reach this criterion over the Monte-Carlo simulation. We use the preconditioner $\mathcal{P}_k$ defined by (4.4) with

Test Problem \ Mesh	16×16	32×32	64×64
1 ($\sigma^2 = 6.0 \times 10^{-3}$)	5.99	5.95	5.83
2 ($\sigma^2 = 6.0 \times 10^{-3}$)	5.78	5.77	5.61
3 (P_2)	4.58	3.93	3.19
4 ($\ell = 1.0$)	4.98	4.32	3.05

	$4 \times 4 \times 4$	$8 \times 8 \times 8$	$16 \times 16 \times 16$
5 (P_2)	5.16	4.88	4.47

Table 4.1: Preconditioned GMRES iteration counts.

$k = \frac{\eta_m}{\mu}$. Direct methods are used to solve the subsidiary systems corresponding to the blocks $kQ_{\mathbf{B}} + A + N$ and $\frac{1}{k}L_{\mathbf{r}}$ in $\mathcal{P}_k$. While direct methods are viable for the small problems investigated in this study, we note that effective multigrid solvers have been developed for systems similar in form to the block $kQ_{\mathbf{B}} + A + N$ (see e.g. [9, 10] and the references therein).

Average iteration counts for each test problem are reported in Table 4.1, each on three different meshes. These results demonstrate that the preconditioner is highly effective for both problems with fluctuations in the velocity field (Test Problems 1 and 2) and those with heterogeneous resistivities (Test Problems 3, 4, and 5). Furthermore, the preconditioner is robust with respect to the mesh, with average iteration counts decreasing as the mesh is refined.

5. Conclusion. We have presented a numerical method for simulating the kinematics of MHD when either the velocity field or the magnetic resistivity of the fluid is uncertain, applying the method to several steady-state test problems. We have modeled the effect of random perturbations in the velocity field on the induced magnetic field. In particular, we have demonstrated that, on average, fluctuations with non-zero vorticity have a large global effect on the induced magnetic field. This supports the theory that small-scale turbulent flow is necessary for dynamo action. These results also suggest that simulations based on mean flow may underpredict the magnitude of magnetic fields. We have also demonstrated that uncertainty in the distribution of the resistivity can result in different magnetic topologies than in the deterministic case. Our results show that this effect is most pronounced when the resistivity in large regions of the domain is uncertain. On the other hand, we have found that, on average, the induced magnetic field is largely insenstive to small-scale fluctuations in the resistivity, even when these fluctuations vary over several orders of magnitude throughout the domain.

In this study, we have introduced several stochastic models for uncertain quantities in the context of MHD kinematics. By expressing the resistivity as a piecewise constant field or a truncated KL expansion, we allow for this quantity to be modeled by a vector of independent random variables. We have also proposed physically motivated expressions for the velocity field that not only couple its components in a natural way but also require the construction of only one random field in two dimensions. We have employed Monte-Carlo simulation to obtain mean and variance data, but the stochastic expressions introduced here can be used directly in more sophisticated uncertainty quantification methods such as stochastic Galerkin, stochastic

collocation, and quasi-Monte-Carlo methods.

In addition, we have developed a preconditioner for the discrete kinematics equations which is robust over variations in both the resistivity and the velocity field. This is important because many linear systems need to be solved in order to obtain accurate probabilistic distributions of the solution $\vec{B}_h$. Because this preconditioner is mesh independent, it allows for the possibility of larger-scale MHD kinematics simulations in both two and three dimensions. Furthermore, this preconditioner can be useful in fully coupled MHD models in which the resistivity and velocity field can fluctuate due to the coupling of the kinematics equations to the Navier-Stokes equations.

REFERENCES

[1] W. Bangerth, T. Heister, G. Kanschat, et al., deal.II *Differential Equations Analysis Library, Technical Reference*. http://www.dealii.org.
[2] R. Caflisch, *Monte Carlo and quasi-Monte Carlo methods*, Acta Numerica, 7 (1998), pp. 1–49.
[3] R. Codina and N. Hernández, *Stabilized finite element approximation of the stationary magneto-hydrodynamics equations*, Computational Mechanics, 38 (2006), pp. 344–355.
[4] M. Costabel and M. Dauge, *Weighted regularization of Maxwell equations in polyhedral domains*, Numerische Mathematik, 93 (2002), pp. 239–277.
[5] P. Davidson, *An Introduction to Magnetohydrodynamics*, Cambridge University Press, 2001.
[6] J.-F. Gerbeau, C. Le Bris, and T. Lelièvre, *Mathematical Methods for the Magnetohydrodynamics of Liquid Metals*, Oxford University Press, 2006.
[7] R. Ghanem and P. Spanos, *Stochastic Finite Elements: A Spectral Approach*, Dover Publications, 2003.
[8] C. Greif and D. Schötzau, *Preconditioners for the discretized time-harmonic Maxwell equations in mixed form*, Numerical Linear Algebra with Applications, 14 (2007), pp. 281–297.
[9] R. Hiptmair and J. Xu, *Nodal auxiliary space preconditioning in H(Curl) and H(Div) spaces*, SIAM Journal on Numerical Analysis, 45 (2007), pp. 2483–2509.
[10] J. Hu, R. Tuminaro, P. Bochev, C. Garasi, and A. Robinson, *Toward an h-independent algebraic multigrid method for Maxwell's equations*, SIAM Journal on Scientific Computing, 27 (2006), pp. 1669–1688.
[11] J. Brown Jr., *Mean square error in series expansions of random functions*, Journal of the Society of Industrial and Applied Mathematics, 8 (1960), pp. 28–32.
[12] J. Liu, S. Tavener, and H. Chen, *ELLAM for resolving the kinematics of two-dimensional resistive magnetohydrodynamic flows*, Journal of Computational Physics, 227 (2007), pp. 1372–1386.
[13] M. Murphy, G. Golub, and A. Wathen, *A note on preconditioning for indefinite linear systems*, SIAM Journal on Scientific Computing, 21 (2000), pp. 1969–1972.
[14] J.-C. Nédélec, *Mixed finite elements in* $\mathbb{R}^3$, Numerische Mathematik, 35 (1980), pp. 315–341.
[15] M. Rao and R. Swift, *Probability Theory with Applications*, Springer, 2006.
[16] N. Ben Salah, A. Soulaimani, and W. Habashi, *A finite element method for magnetohydrodynamics*, Computational Methods in Applied Mechanics and Engineering, 190 (2001), pp. 5867–5892.
[17] D. Schötzau, *Mixed finite element methods for stationary incompressible magnetohydrodynamics*, Numerische Mathematik, 96 (2004), pp. 771–800.